

Drosonde Observations of Total Integrated Water Vapor Transport within North Pacific Atmospheric Rivers

F. M. RALPH,^a S. F. IACOBELLIS,^a P. J. NEIMAN,^b J. M. CORDEIRA,^c J. R. SPACKMAN,^{b,d}
D. E. WALISER,^e G. A. WICK,^b A. B. WHITE,^b AND C. FAIRALL^b

^a *Center for Western Weather and Water Extremes, Scripps Institution of Oceanography,
University of California, San Diego, La Jolla, California*

^b *NOAA/OAR/ESRL/Physical Sciences Division, Boulder, Colorado*

^c *Plymouth State University, Plymouth, New Hampshire*

^d *Science and Technology Corporation, Boulder, Colorado*

^e *NASA Jet Propulsion Laboratory, Pasadena, California*

(Manuscript received 3 March 2017, in final form 5 July 2017)

ABSTRACT


Aircraft drosonde observations provide the most comprehensive measurements to date of horizontal water vapor transport in atmospheric rivers (ARs). The CalWater experiment recently more than tripled the number of ARs probed with the required measurements. This study uses vertical profiles of water vapor, wind, and pressure obtained from 304 drosondes across 21 ARs. On average, total water vapor transport (TIVT) in an AR was $4.7 \times 10^8 \pm 2 \times 10^8 \text{ kg s}^{-1}$. This magnitude is 2.6 times larger than the average discharge of liquid water from the Amazon River. The mean AR width was $890 \pm 270 \text{ km}$. Subtropical ARs contained larger integrated water vapor (IWV) but weaker winds than midlatitude ARs, although average TIVTs were nearly the same. Mean TIVTs calculated by defining the lateral “edges” of ARs using an IVT threshold versus an IWV threshold produced results that differed by less than 10% across all cases, but did vary between the midlatitudes and subtropical regions.

1. Introduction

The global atmospheric water budget is a subject of ongoing research. Recent evaluations of global climate model representations of precipitation, evaporation, and moisture transport compared to observed river discharges into oceans (Trenberth et al. 2011) concluded that “their differences reveal outstanding issues with atmospheric models and their biases.” One reason for their differences is that horizontal water vapor transport in climate models is sensitive to grid size (e.g., Hughes et al. 2012; Demory et al. 2014). Demory et al. (2014) notes that “as [model] resolution is increased, precipitation decreases over the ocean and increases over the land. This is associated with an increase in atmospheric moisture transport from ocean

to land, which changes the partitioning of moisture fluxes that contribute to precipitation over land from less local to more nonlocal moisture sources.” This reasoning raises the question of what amount of water vapor transport is correct, and thus how well atmospheric rivers (ARs) are represented, since they are responsible for 90% or more of horizontal water vapor transport in the midlatitudes (e.g., Zhu and Newell 1998; Ralph et al. 2004). To help address this challenge, the data and analyses presented herein use field observations from research aircraft during the recent CalWater field experiments (Ralph et al. 2016) and from earlier experiments. The CalWater data more than triple the number of suitably observed cases available.

The crucial role of ARs in determining the water vapor and precipitation distribution and variability in and near the midlatitudes makes them a key player in the water cycle. These relatively narrow (<1000 km), low-altitude (75% of water transport within lowest 2.5 km), elongated (>~2000 km) corridors of strong horizontal water vapor transport occur over most midlatitude areas

 Denotes content that is immediately available upon publication as open access.

Corresponding author: F. Martin Ralph, mralph@ucsd.edu

of the globe (Waliser et al. 2012). Their impacts are becoming increasingly recognized, particularly for the western, and even central, United States, as well as other areas in the world where they are implicated in extreme precipitation and most major flooding events on the west coasts of midlatitude continents (Ralph et al. 2006, 2011; Neiman et al. 2008a,b, 2011; Leung and Qian 2009; Guan et al. 2010, 2013; Dettinger et al. 2011; Lavers et al. 2011, 2012; Moore et al. 2012; Kim et al. 2013; Viale and Nunez 2011). For example, Ralph et al. (2006) showed that the seven largest mean daily flow events during the 1997–2006 period on Northern California’s Russian River are directly attributed to heavy precipitation during landfalling ARs. Similarly, Neiman et al. (2011) showed most annual peak streamflow events in Washington were associated with ARs. Studies in Europe (Stohl et al. 2008; Lavers et al. 2011, 2012) and South America (Viale and Nunez 2011) have come to similar conclusions. In conjunction with these flooding hazards, ARs also make vital contributions to the regional water supply and can be key in breaking droughts. For example, 25%–50% of the water supply (i.e., snowpack and rain) in the U.S. West Coast states is delivered by only a few AR events (Guan et al. 2010; Dettinger et al. 2011; Ralph et al. 2013), and roughly 40% of drought breaks in California were associated with a period of landfalling ARs (Dettinger 2013). Additionally, recent diagnoses of new climate projections of annual precipitation in California have found that the largest contributor to intermodel variability in this key parameter is caused by how the strongest precipitation events (i.e., in this area, ARs) are represented (Pierce et al. 2013).

Most earlier AR studies have depended upon satellite-observed vertically integrated water vapor (IWV) using Special Sensor Microwave Imager (SSM/I) satellite data (e.g., Ralph et al. 2004; Wick et al. 2013), or on reanalyses and model-derived analyses (e.g., Neiman et al. 2008a; Lavers et al. 2011; Cordeira et al. 2013). Although the IWV measurements provide a useful proxy for AR water vapor transport, anecdotal evidence suggests there are numerous instances when the IWV measurements identify an AR in the presence of very little horizontal water vapor transport occurring (often in the “equatorward tail” of an IWV AR signature).

In spite of their importance, very few measurements have been available to observationally quantify and validate the amount of water vapor *transported* in ARs. These validations have focused on case studies in which dropsondes released from research aircraft across an AR are used to determine the horizontal water vapor

transport (Ralph et al. 2004, 2005, 2011; Neiman et al. 2014). The dropsondes measure wind, water vapor, temperature, and pressure as they descend. One of the goals of the CalWater program of field studies (Ralph et al. 2016) has been to collect a much larger set of such observations so as to better quantify and understand ARs over the Pacific Ocean. This paper presents analyses combining the earlier flight data with the new CalWater measurements. Additionally, these data allow for quantitative comparison of the well-established IWV-based threshold (20 mm) used to define the lateral “edges” of an AR with the emerging use of an integrated vapor transport (IVT) threshold [typically $250 \text{ kg m}^{-1} \text{ s}^{-1}$; e.g., Moore et al. (2012) and Rutz et al. (2014), though Mahoney et al. (2016) uses $500 \text{ kg m}^{-1} \text{ s}^{-1}$ for the southeast United States (a region with greater background water vapor), and a variable IVT threshold was used by Lavers et al. (2012) and Guan and Waliser (2015)].

In February 2014, the NOAA Gulfstream IV-SP (G-IV) research aircraft sampled 10 ARs over the northeast Pacific Ocean as part of an “early start” deployment for the CalWater2 project. On five of these flights, multiple dropsondes were deployed in a line crossing the AR to sample the total AR water vapor transport (AR transport). During the main deployment of CalWater2, the NOAA G-IV aircraft sampled transects across another seven ARs in early 2015 while the U.S. Air Force Lockheed C-130 Hercules (USAF C-130) sampled four ARs in early 2016. These recent data more than quadrupled the overall number of such cross-AR airborne samples suitable for calculating AR water vapor transport. The sampling also allowed for analysis to explore what number of dropsonde samples is needed to accurately quantify the full water vapor transport of an AR through a cross section across an AR. The “AR transport” is defined here as the total IVT (TIVT) and is calculated as the horizontal integral of IVT across the AR transect perpendicular to the direction of mean vapor transport. Analysis of these 12 new samples, in combination with the five previous samples from the preceding 10 years, from a Hawaii-based experiment in 2005 (Ralph et al. 2011) and Winter Storms and Pacific Atmospheric Rivers (WISPAR) in 2011 (Neiman et al. 2014), are used here to comprehensively investigate the observed amount of water vapor transport in ARs and to compare IWV-based and IVT-based AR detection criteria.

2. Data

Vertical profiles of dropsonde measurements gathered from 37 research flights that observed ARs over the

TABLE 1. List of research flights used in this study. Included in the table are the number of dropsondes within the criteria noted in the main text. CALJET = California Landfalling Jets Experiment. USAF C-130 flights were flown out of Hickam AFB (H) or McChord AFB (M), California.

	Date (UTC at initial dropsonde)	Campaign	Aircraft	No. of usable sondes
1	25 Jan 1998	CALJET	NOAA P-3	25
2	24 Mar 2005	Ghostnets	NOAA P-3	33
3	26 Mar 2005	Ghostnets	NOAA P-3	23
4	11 Feb 2011	WISPAR	NASA Global Hawk	19
5	3 Mar 2011	WISPAR	NOAA G-IV	42
6	3 Mar 2011	WISPAR	NASA Global Hawk	59
7	9 Mar 2011	WISPAR	NASA Global Hawk	56
8	7 Feb 2014	CalWater2-Pre	NOAA G-IV	23
9	8 Feb 2014	CalWater2-Pre	NOAA G-IV	29
10	11 Feb 2014	CalWater2-Pre	NOAA G-IV	37
11	12 Feb 2014	CalWater2-Pre	NOAA G-IV	15
12	13 Feb 2014	CalWater2-Pre	NOAA G-IV	23
13	14 Feb 2014	CalWater2-Pre	NOAA G-IV	4
14	15 Feb 2014	CalWater2-Pre	NOAA G-IV	14
15	18 Feb 2014	CalWater2-Pre	NOAA G-IV	14
16	19 Feb 2014	CalWater2-Pre	NOAA G-IV	12
17	21 Feb 2014	CalWater2-Pre	NOAA G-IV	17
18	22 Feb 2014	CalWater2-Pre	NOAA G-IV	4
19	25 Feb 2014	CalWater2-Pre	NOAA G-IV	4
20	15 Jan 2015	CalWater2	NOAA G-IV	24
21	17 Jan 2015	CalWater2	NOAA G-IV	29
22	22 Jan 2015	CalWater2	NOAA G-IV	13
23	24 Jan 2015	CalWater2	NOAA G-IV	23
24	5 Feb 2015	CalWater2	NOAA G-IV	8
25	6 Feb 2015	CalWater2	NOAA G-IV	29
26	8 Feb 2015	CalWater2	NOAA G-IV	31
27	14 Feb 2015	CalWater2	NOAA G-IV	40
28	20 Feb 2015a	CalWater2	NOAA G-IV	37
29	20 Feb 2015b	CalWater2	NOAA G-IV	28
30	22 Feb 2015	CalWater2	NOAA G-IV	30
31	24 Feb 2015	CalWater2	NOAA G-IV	35
32	13 Feb 2016	CalWater2	USAF C-130 (H)	51
33	13 Feb 2016	CalWater2	USAF C-130 (M)	47
34	15 Feb 2016	CalWater2	USAF C-130 (M)	41
35	15 Feb 2016	CalWater2	USAF C-130 (H)	39
36	21 Feb 2016	CalWater2	USAF C-130 (M)	37
37	21 Feb 2016	CalWater2	USAF C-130 (H)	57
			Total	1052

Northeast Pacific Ocean during the 1998–2016 period were examined (Table 1). To be considered in the present analysis, each profile was required to have no vertical data gaps exceeding 50 hPa within the surface-to-500-hPa layer. Applying this criterion yielded a total of 1052 profiles of dropsonde measurements, with the number of dropsondes per flight varying from 4 to 59. The IWV and IVT were calculated from each profile using

$$IWV = \frac{1}{g} \int_{p_{\text{stc}}}^{p_{\text{top}}} q dp$$

and

$$IVT = \frac{1}{g} \int_{p_{\text{stc}}}^{p_{\text{top}}} q \mathbf{V} dp,$$

where g is gravity, q is the specific humidity, \mathbf{V} is the wind velocity, and p_{top} is the upper limit of data from each dropsonde. The value of p_{top} varies among the dropsondes, thus impacting comparison of calculated values of IWV and IVT. We assume this impact is not significant since we required dropsondes to provide data throughout the surface-to-500-hPa layer that contains the vast majority of atmospheric water vapor (e.g., only 3% of the total atmospheric water vapor and 5% of the total IVT was contained in the 500–200-hPa layer based on 400 dropsondes with data extending above 200 hPa).

TABLE 2. Flight information and derived atmospheric properties from the 17 AR transects used in this study. The width and TIVT of each AR were calculated using both IWV (subscript *a*) and IVT (subscript *b*) critical thresholds of 20 mm and 250 kg m⁻¹ s⁻¹, respectively. The first column is the case number, which is chronological. The date corresponds to the midpoint of each transect. The mean direction is defined using the vertically integrated (from surface to top of sounding) *u* and *v* components of IVT. The cases are separated into those from the subtropics (centered from roughly 23° to 33°N) and those from the midlatitudes (centered from roughly 33° to 43°N), and statistics of each subset are provided. The bottom two rows contain the mean and standard deviations for all 17 transects.

Case No.	Date	Aircraft	Start/end time	Central lon	Central lat	No. of sondes ^a	Mean dir.	IWV _{MAX} (mm)	IVT _{MAX} (kg m ⁻¹ s ⁻¹)	TIVT _a (10 ⁸ kg s ⁻¹)	Width _a (km)	TIVT _b (10 ⁸ kg s ⁻¹)	Width _b (km)
Subtropical													
1	25 Mar 2005	P-3	0040–0300 UTC	156.2°W	27.2°N	16	233	41.2	674	4.26	1196	3.96	1016
2	12 Feb 2011	G-Hawk	0558–0726 UTC	145.9°W	27.7°N	9	237	41.0	585	2.37	811	1.77	415
3	04 Mar 2011	G-IV	0003–0302 UTC	163.4°W	23.0°N	17	220	48.9	725	4.85	1539	4.24	849
6	08 Feb 2014	G-IV	2243–2338 UTC	139.3°W	31.0°N	9	230	41.7	1029	3.44	602	3.56	611
10	19 Feb 2014	G-IV	2312–0158 UTC	151.7°W	27.5°N	11	203	39.6	314	3.54	1802	1.33	477
15	14 Feb 2015	G-IV	1823–1928 UTC	152.3°W	24.2°N	11	229	46.1	1204	6.62	846	6.87	917
16	20 Feb 2015	G-IV	0012–0154 UTC	156.7°W	27.0°N	13	240	41.7	861	5.19	964	5.63	1092
17	22 Feb 2015	G-IV	2152–2330 UTC	160.8°W	31.0°N	17	232	39.1	926	6.94	1334	6.30	1026
21	21 Feb 2016	C-130	2037–0004 UTC	149.6°W	29.1°N	24	208	32.7	942	7.08	1202	8.33	1354
				Mean (subtropical cases)		14	226	41.3	807	4.92	1144	4.67	862
				Standard deviation		4.6	12	4.3	249	1.59	359	2.19	291
Midlatitude													
4	04 Mar 2011	G-Hawk	1102–1340 UTC	134.7°W	41.5°N	10	231	18.1	531	— ^b	— ^b	2.46	687
5	09 Mar 2011	G-Hawk	2240–0022 UTC	131.1°W	40.4°N	15	226	25.0	622	1.92	382	3.26	723
7	11 Feb 2014	G-IV	1903–2124 UTC	134.0°W	42.1°N	23	232	37.4	1296	7.94	1035	8.05	1067
8	12 Feb 2014	G-IV	1734–1903 UTC	125.5°W	40.8°N	14	245	32.0	636	3.21	808	2.80	619
9	13 Feb 2014	G-IV	1833–2058 UTC	133.0°W	42.5°N	21	220	33.2	789	4.39	733	6.90	1371
11	15 Jan 2015	G-IV	2114–2222 UTC	127.3°W	41.8°N	9	219	27.4	733	3.21	639	3.45	692
12	17 Jan 2015	G-IV	2245–0030 UTC	130.2°W	41.6°N	10	236	28.4	831	4.17	603	6.11	1154
13	24 Jan 2015	G-IV	2148–2254 UTC	139.6°W	38.2°N	12	203	29.9	607	2.58	534	3.74	868
14	08 Feb 2015	G-IV	1328–1448 UTC	124.6°W	34.9°N	11	216	34.8	938	4.35	774	5.96	1054
18	13 Feb 2016	C-130	2055–2250 UTC	152.7°W	40.0°N	19	229	29.7	798	3.50	515	5.16	963
19	14 Feb 2016	C-130	2341–0158 UTC	142.0°W	43.0°N	23	241	32.5	954	5.93	875	6.82	1143
20	15 Feb 2016	C-130	2107–2221 UTC	130.5°W	46.4°N	10	242	23.0	554	1.18	222	2.22	514
				Mean (midlatitude cases)		15	228	29.3	774	3.85	647	4.74	905
				Standard deviation		5	12	5.1	207	1.79	221	1.91	250
				Overall mean		14.5	227	34.4	788	4.33	871	4.71	886
				Overall standard deviation		4.9	12	7.6	227	1.78	382	2.04	269

^a Number of sondes in AR transect.

^b No dropsondes satisfied the IWV > 20 mm threshold.

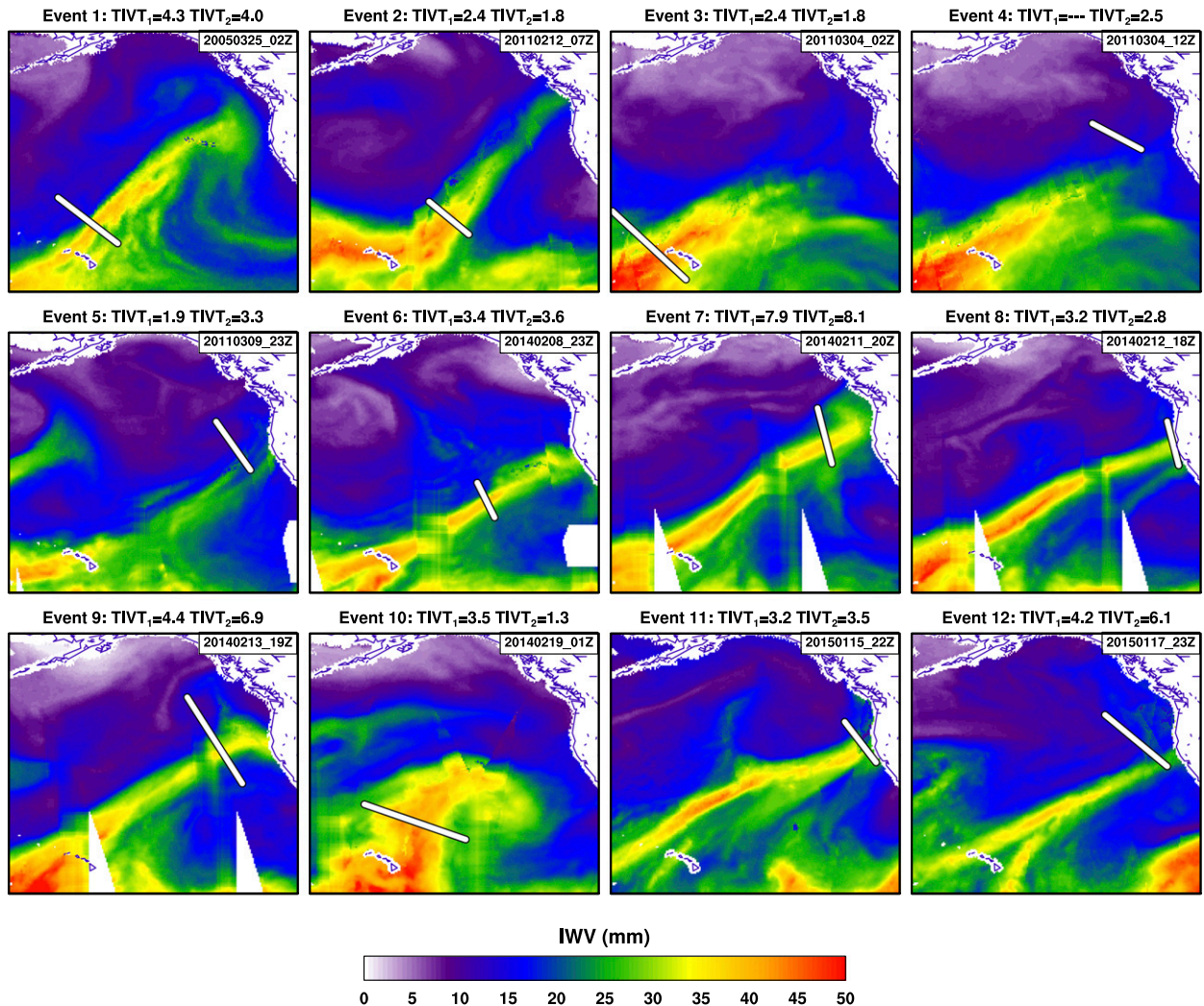


FIG. 1. Composite SSM/I satellite imagery of IWV during AR events 1–12 listed in Table 2. Composites formed using available SSM/I data within ± 16 h of transect time. The white lines represent the approximate location of each AR transect. The image times (upper-right corner of each panel) were selected to correspond as close as possible to the midpoint of each transect. The total vapor transport within each AR using both IWV ($TIVT_1$) and IVT ($TIVT_2$) critical thresholds are listed above each panel. White areas denote either land pixels or missing data. Some of the IWV imagery contains artifacts that result from the blending of data ± 16 h of the transect time. SSM/I data were produced by Remote Sensing Systems and accessed at www.remss.com.

The AR water vapor transport is calculated from transects that meet the following three criteria:

- transect had to consist of at least nine dropsondes (to help insure adequate observational coverage of the AR core; see section 3e for an assessment of sensitivity of TIVT to dropsonde spacing),
- $IWV > 20 \text{ mm}$ or $|IVT| > 250 \text{ kg m}^{-1} \text{ s}^{-1}$ at a minimum of three interior dropsonde locations, and
- $IWV < 20 \text{ mm}$ or $|IVT| < 250 \text{ kg m}^{-1} \text{ s}^{-1}$ at both ends of the transect.

The threshold value of $IWV = 20 \text{ mm}$ is motivated by Ralph et al. (2004) and Neiman et al. (2008a),

whereas the threshold value of $|IVT| = 250 \text{ kg m}^{-1} \text{ s}^{-1}$ is motivated by Moore et al. (2012) and Rutz et al. (2014).

Application of these conditions to the dropsonde data from the 37 flights in Table 2 yielded 21 individual transects (total of 304 dropsondes) deemed to contain enough observations to adequately sample an AR cross section. However, in some of these 21 cases the dropsonde transect did not extend far enough away from the center on one side (usually the equatorward side) to completely sample the AR using the above IWV and IVT criteria. In other words, the first or last dropsonde in the transect was still within the AR using the $IWV > 20 \text{ mm}$ and $IVT > 250 \text{ kg m}^{-1} \text{ s}^{-1}$

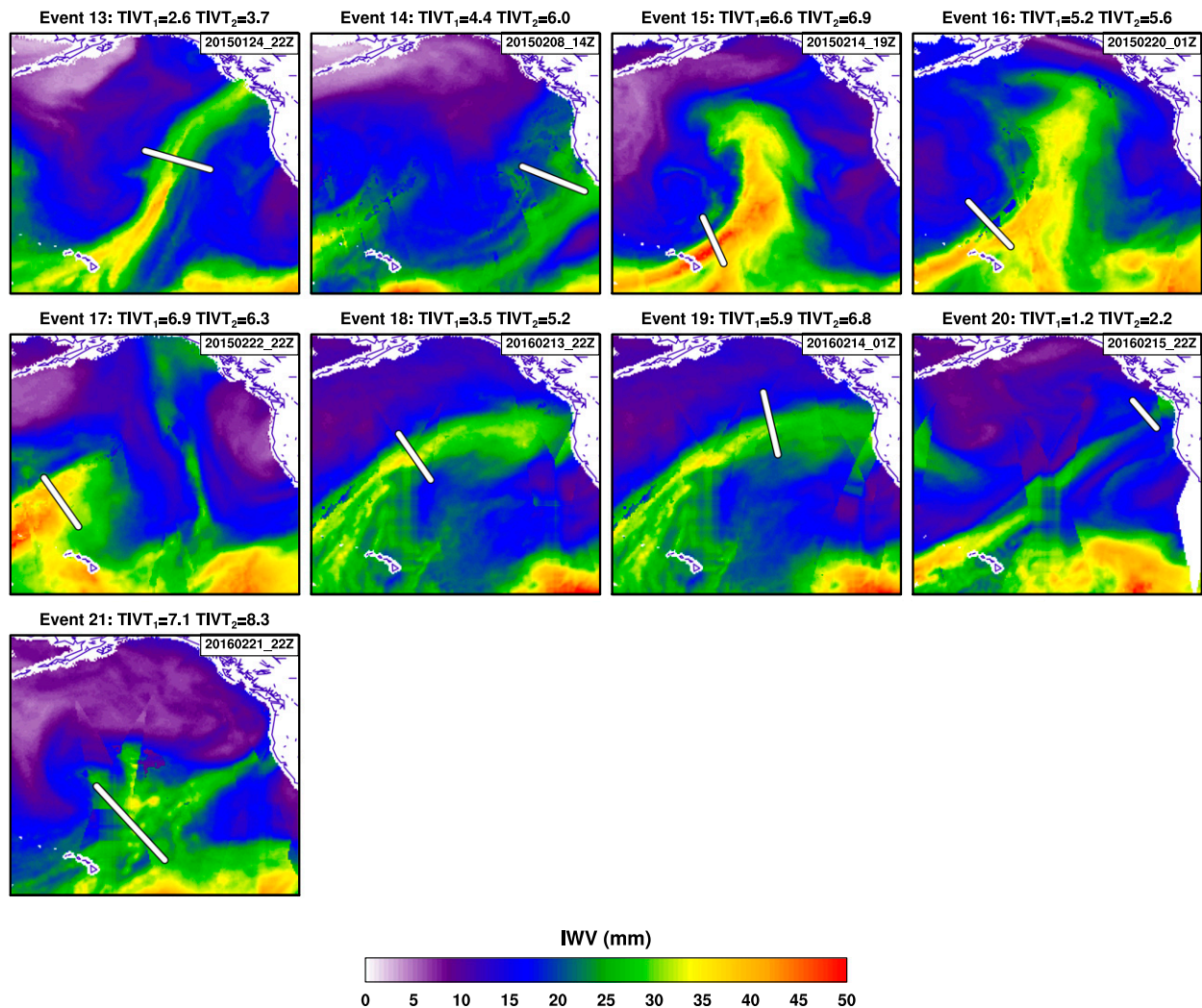


FIG. 2. As in Fig. 1, but for AR events 13–21 listed in Table 2.

thresholds. To increase the number of available study cases, the criteria were subjectively relaxed. This resulted in four subcategories of cases:

- 1) AR defined using stated IWT and IVT thresholds (seven cases).
- 2) Lateral edges defined if first or last dropsonde reported IWT and/or IVT within 15% of respective threshold (six cases).
- 3) Lateral edge of equatorward side of AR defined using IVT threshold but not IWT threshold (four cases). All of these were subtropical cases where the equatorward boundary of the AR was within a large region of high IWT based on SSM/I IWT imagery. This suggests that the main advective dynamics associated with the AR was completely sampled by the dropsondes and also illustrates a drawback to using the IWT threshold in these subtropical regions.

- 4) A lateral edge of AR not defined using IVT threshold but numerical model analyses indicates that lateral edge of AR was within 200 km of end of dropsonde transect (four cases). For these cases, calculations of TIVT and AR width using Global Forecast System (GFS) 0.5° analysis products (EMC 2003) were performed along (i) the partial transect defined by the available dropsondes and (ii) the full transect with the missing AR edge defined from GFS IVT values using the analysis time closest to the time at midtransect. Comparison of calculations (i) and (ii) indicate that using the partial transect defined by the available dropsondes results in underestimates of 8% in TIVT and 16% in AR width.

Separate calculations of TIVT (as well as other variables) are made for each of the thresholds used to determine AR boundaries: 1) $IWT > 20 \text{ mm}$ or 2) $IVT > 250 \text{ kg m}^{-1} \text{ s}^{-1}$ for transects that occur in the

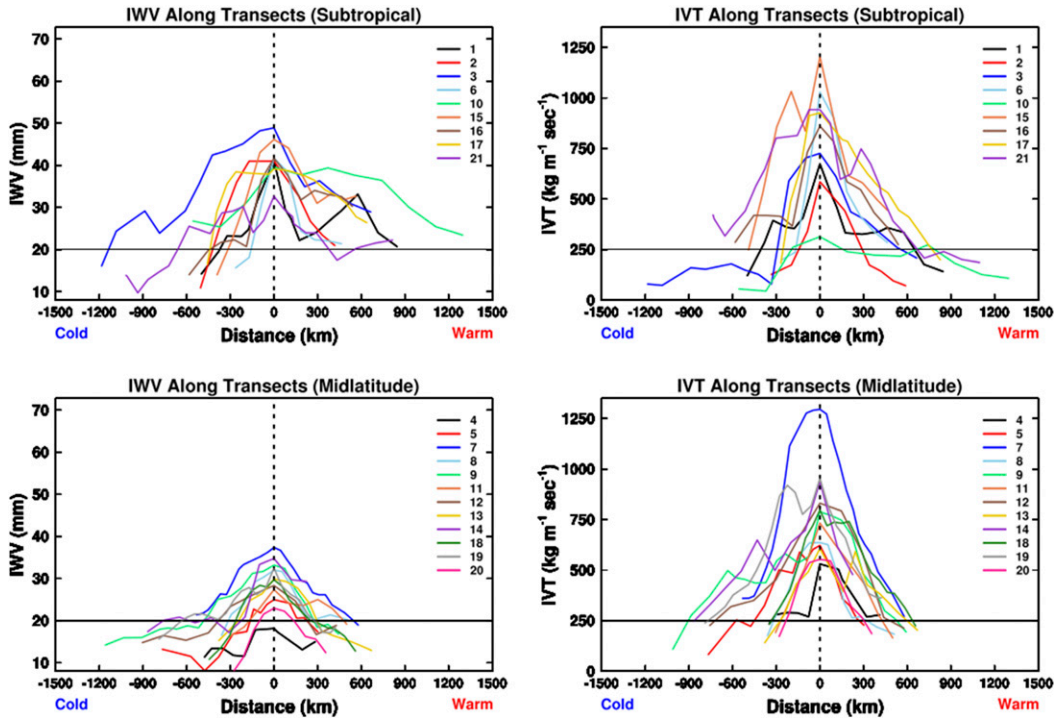


FIG. 3. (left) IWP and (right) IVT calculated along each transect listed in Table 2. Transects are grouped by location: (top) subtropical and (bottom) midlatitude. The horizontal distance scale is referenced to the dropsonde location with the largest value of IWP or IVT in each transect. Transects are oriented with the cold end (generally toward the northwest) located on the left side of the plots. The horizontal black lines represent the critical IWP and IVT thresholds (see text) used to identify the presence of an AR.

subtropics (central latitude < 33°N) and midlatitudes (central latitude > 33°N).

The large-scale spatial distributions of SSM/I-derived IWP (Wentz et al 2012) at the time of each transect

are shown in Figs. 1 and 2, whereas the transect values of IWP and IVT magnitude are shown in Fig. 3. Examination of many of the SSM/I-derived IWP analyses illustrate a well-defined corridor of enhanced IWP that

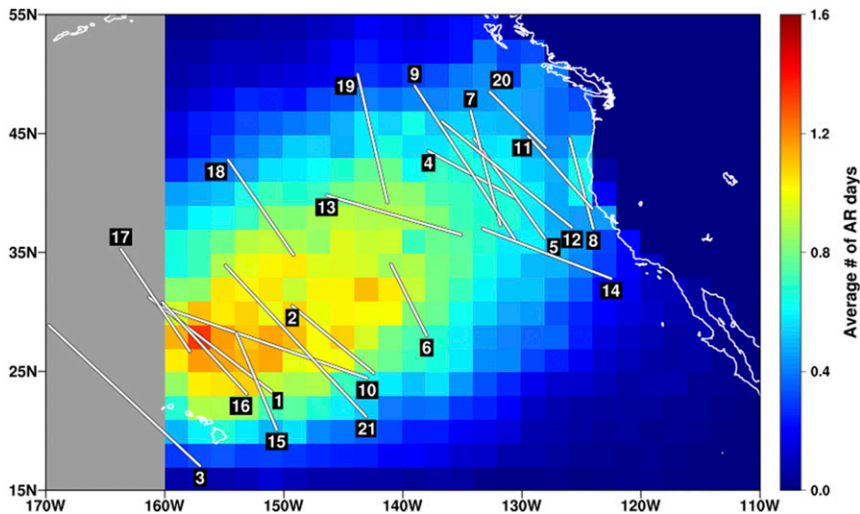


FIG. 4. Location of the dropsonde transects listed in Table 1 (transect numbers, per Table 1, are shown). The background image denotes weekly AR frequency calculated using the AR detection tool of Wick et al. (2013) applied during the 2003–12 cool seasons (November–February). AR frequency data west of 160°W were not available.

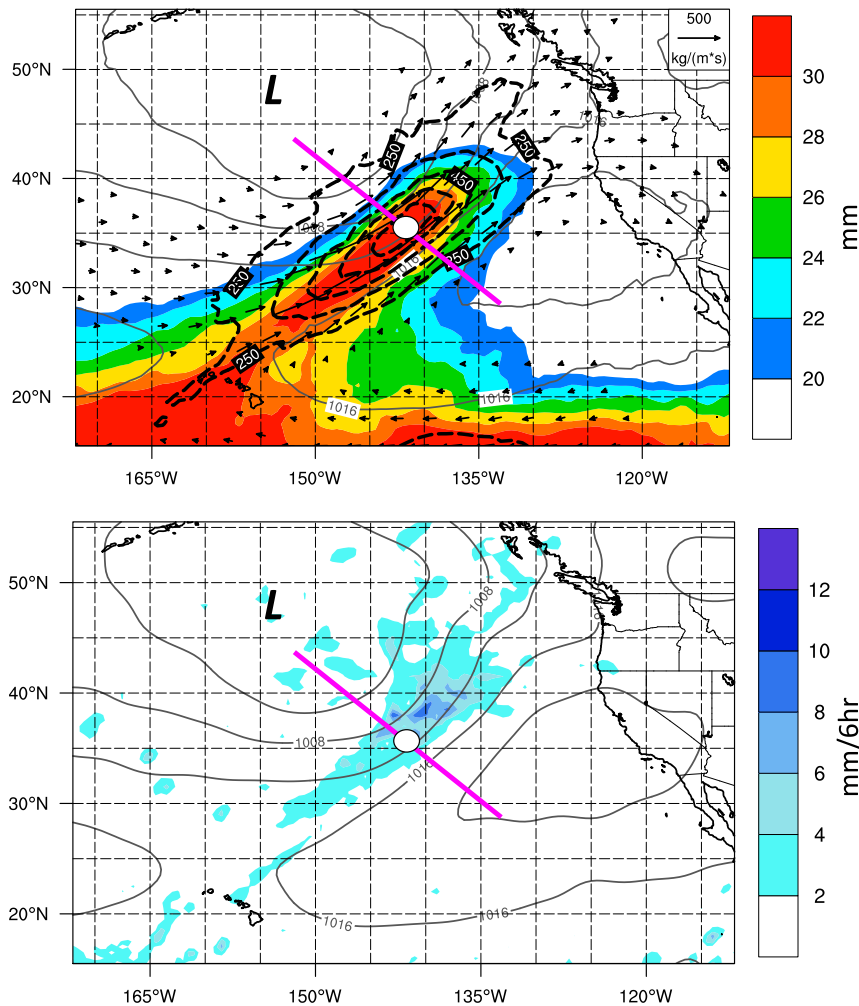


FIG. 5. AR composite from 21 cases observed over the eastern North Pacific Ocean. Gridded plan view composite derived from gridded GFS reanalysis data with mean central position of all 21 cases denoted by white dot and composite. (top) Composite IWT (mm; color fill), IVT direction (vectors), and magnitude ($\text{kg m}^{-1} \text{s}^{-1}$; dashed black contours at intervals of $50 \text{ kg m}^{-1} \text{s}^{-1}$ and vector length) and (bottom) composite precipitation rate. In both panels the composite mean sea level pressure (hPa) is denoted by the thin solid contours.

is a common signature of an AR (e.g., Ralph et al. 2004; Neiman et al. 2008a,b), whereas examination of the transect values of IVT magnitude reveals that each transect contains IVT magnitudes $> 250 \text{ kg m}^{-1} \text{s}^{-1}$. Transects are mostly found over the eastern North Pacific between 17° and 49°N in a location that frequently experiences AR conditions during winter months (Fig. 4).

3. Analysis

a. Overall mean and comparison of IWT- and IVT-based methods

The 21-case mean TIVT is $4.7 \times 10^8 \text{ kg s}^{-1}$, using the IVT magnitude threshold of $250 \text{ kg m}^{-1} \text{s}^{-1}$; the IWT

threshold of 2 cm yielded an average TIVT that was 8% smaller. The average AR width is 886 km using the IVT magnitude threshold, which is just 2% larger than that derived using the IWT threshold [note that the width is greater than that of Ralph et al. (2004) because that study limited cases to those $< 1000 \text{ km}$ wide and did not address subtropical cases as much; as shown in Table 2, the subtropical cases are much broader than are the midlatitude cases—1144 km versus 647 km]. The small differences obtained using the two thresholding methods indicate that the IVT magnitude threshold of $250 \text{ kg m}^{-1} \text{s}^{-1}$ corresponds well to the well-established IWT threshold of 2 cm. The IVT magnitude threshold method has some distinct advantages when the AR transects are subdivided by

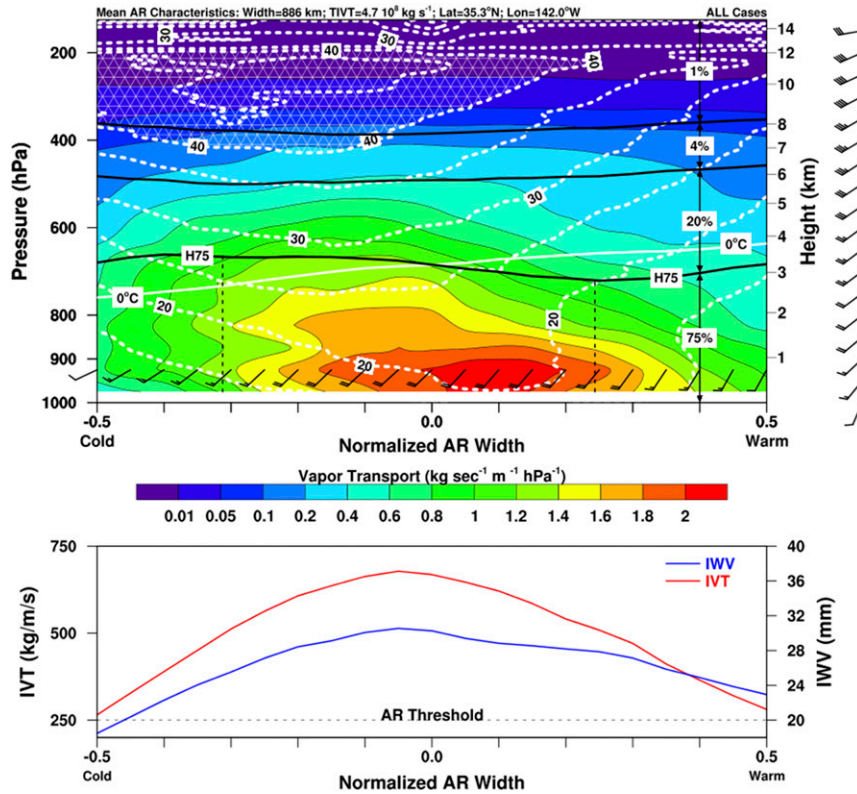


FIG. 6. AR composite cross section based on dropsonde data from the 21 cases observed over the eastern North Pacific Ocean derived by normalizing the horizontal width of each transect to match the mean width of 860 km (baseline shown as purple line in Fig. 4). (top) Observed composite vertical cross section. Color contours represent the magnitude of the local horizontal water vapor transport, which has been normalized to match the mean TIVT of all 21 ARs. Mean wind speed (dashed white contours; $>40 \text{ m s}^{-1}$ hatched). Freezing level (solid white line), vertical position of H75, and 925-hPa wind speed and direction (barbs = 5 m s^{-1} and half barbs = 2.5 m s^{-1}) are also shown. Horizontal layers containing 75%, 20%, 4%, and 1% of the TIVT are marked. (bottom) Mean cross-AR profiles of IVT and IWV.

latitude. First, the IVT magnitude threshold is less sensitive to varying background IWV conditions as evidenced by the 77% greater average width of ARs in the subtropics as compared to ARs in the midlatitudes using the IWV threshold and a 5% reduced average width of ARs in the subtropics as compared to ARs in the midlatitudes using the IVT magnitude threshold. Second, the IVT magnitude threshold produces results that are far more consistent between subtropical and midlatitude conditions (i.e., the average TIVT and AR widths differ between the regions by 1% and 5%, respectively, for the IVT method, compared to 24% and 77% using the IWV method). Third, orographic precipitation, which is an important driver for both total annual precipitation and individual extreme precipitation events on many west coasts of continents, is driven much more by the flux of water

vapor up a mountain slope (i.e., the upslope component of IVT) than by simply the amount of water vapor (IWV).

b. Comparison of all individual AR transects

The 21 individual transects, shown in Fig. 3, represent an extensive range of ARs as measured by the characteristics listed in Table 2 and by their structures in IWV seen in Figs. 1 and 2. In some cases the IWV criteria were not met, but IVT was (e.g., AR 4), while in others the IWV criteria were met, but the IVT criterion was only barely met (e.g., AR 10). Generally, the subtropical ARs did not have a well-defined southern (warm) edge based on IWV criteria, but did for the IVT criterion. AR 3 had a broad region of large IWV but very weak IVT on its cold side, and the case with the strongest IVT (AR 7) had only

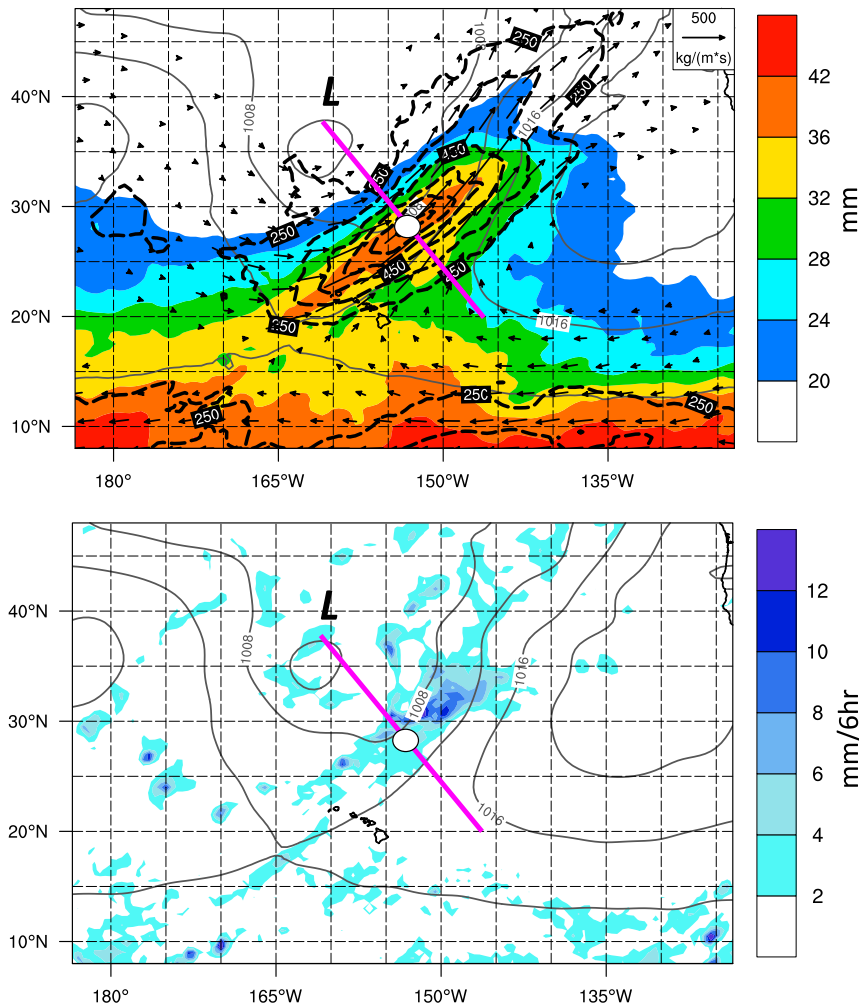


FIG. 7. As in Fig. 5, but for the 9 subtropical cases.

slightly greater maximum IWV than other ARs. Conversely, an IVT magnitude transect with relatively small values (AR 10) has IWV values that are larger than many other transects over much of its width. These differences highlight the importance of the horizontal wind field and how IVT provides a more robust criterion for identifying ARs. The analysis hereafter focuses on the application of IVT magnitude threshold method.

c. Composite AR characteristics

To best synthesize the information from the many AR observations, the data from all 21 transects are averaged into one composite transect. Thus, this transect represents the mean characteristics of the width and TIVT of all the cases observed. To provide the synoptic context, a composite of the plan view perspective is also shown. The resulting composite analysis

(methodology described below) based on all 21 ARs is provided in Figs. 5 and 6. Separate composite analyses for subtropical and midlatitudes cases are shown in Figs. 7–10.

Plan view composites (Figs. 5, 7, 9) were produced using Climate Forecast System (CFS) products (reanalysis for 2005 and 2011 ARs and operational analyses for 2014–16 ARs) at 0.5° resolution. IWV and IVT were computed from 1000 to 250 hPa for each AR listed in Table 2. Composites were formed by referencing (without rotation) the horizontal IWV, IVT, and surface pressure fields to the latitude and longitude of the IVT maximum for each AR.

Cross-sectional view composites (Figs. 6, 8, 10) were produced using dropsonde measurements for each AR. For the vertical cross-section view, IVT was calculated as a function of pressure and horizontal distance along each AR transect and then normalized

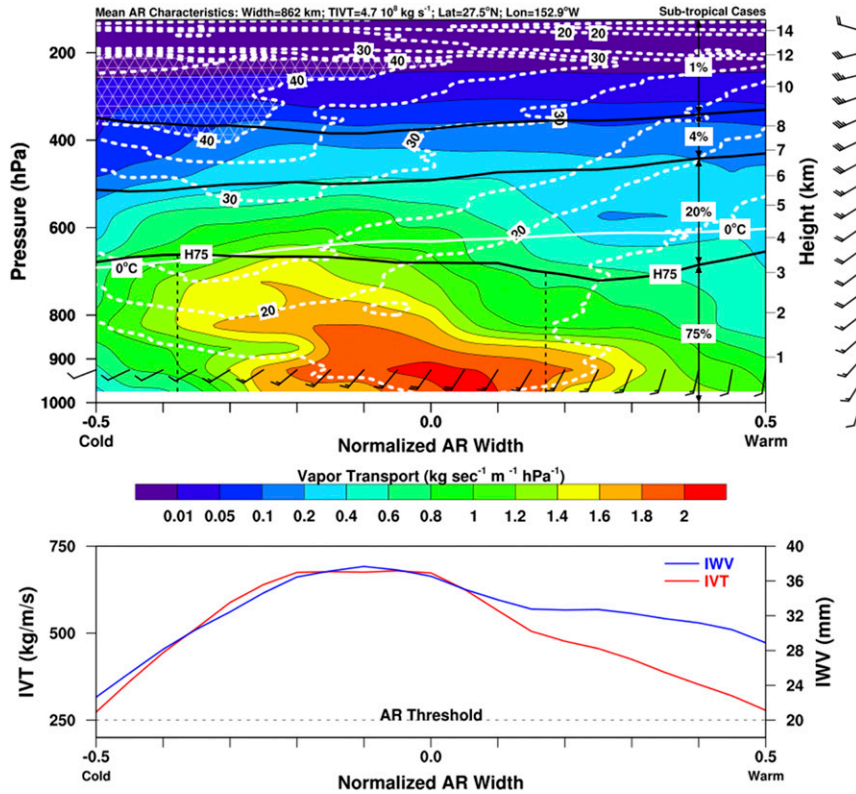


FIG. 8. As in Fig. 6, but for the 9 subtropical cases.

to match the mean width and mean TIVT of all ARs considered. The along-transect vertically integrated IVT and IWV from each AR was normalized to the AR width.

On average, an AR is associated with an extratropical cyclone and is located ~1000 km southeast of the parent low-pressure center (Fig. 5). The regions of composite IVT magnitudes > 250 kg m⁻¹ s⁻¹ and precipitation rates > 2 mm (6 h)⁻¹ extend ~2500 km from southwest to northeast and are embedded within a 3500-km-long region of IWV > 2 cm oriented from southwest to northeast (these lengths are shortened by the compositing method, because it does not rotate the original reanalysis fields from each case). The composite maximum IVT magnitude is ~500 kg m⁻¹ s⁻¹, the maximum IWV is >3 cm, and maximum precipitation rate is 8–10 mm (6 h)⁻¹. The composite IWV pattern looks remarkably similar to a typical SSM/I satellite image. The composite vertical cross section (Fig. 6, top panel) shows the vertically sloping character (upward toward the cold side) of the core of the horizontal water vapor flux above ~900 hPa. The baroclinicity of the region is indicated by the slope of the freezing level, which descends more than 1 km on average across the AR, and by the presence of an

upper-level jet stream wind maximum > 45 ms⁻¹. Most (75%) of the IVT (i.e., H75) is found below about 2.9 km MSL, and the region of the upper-level jet stream wind above 8 km contains just 5% of the IVT. The rather symmetric distribution of IVT across the AR is evident in the bottom panel of Fig. 6. The close correspondence of the IWV-based (2 cm) and IVT-based threshold (250 kg m⁻¹ s⁻¹) on the northwest (cold) edge of the AR is seen in this figure, as is the lack of correspondence at the southeastern (warm) edge.

Table 2, Fig. 3, and Figs. 7–10 reveal some important differences between subtropical and midlatitude ARs. In particular, note that the maximum IWV values in the subtropical cases averaged 41% more than the midlatitudes cases (41.3 versus 29.3 mm), likely due to the general equatorward increase in IWV. In contrast, the average maximum IVT, the average TIVT, and the average width in the midlatitudes all varied by less than 5% from the average values in the subtropics (using IVT threshold method). This difference results largely from the fact that winds are often much stronger in the midlatitude events (mean maximum 925-hPa wind speed was 30.2 ms⁻¹ in midlatitude transects versus 22.0 ms⁻¹ in subtropical transects),

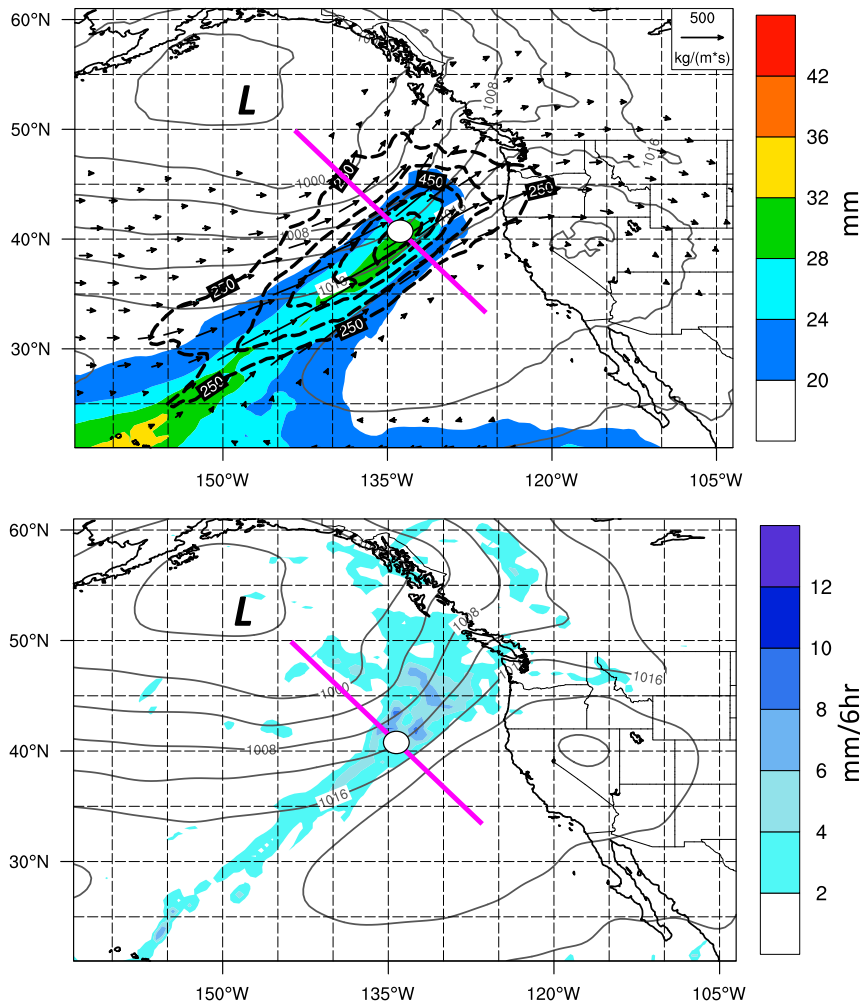


FIG. 9. As in Fig. 5, but for the 12 midlatitude cases.

although the average direction of the full-layer mean transport is nearly identical (226° versus 228°), that is, transporting water vapor from the southwest to northeast. The precipitation distributions also differ, with the midlatitude composite showing structure characteristic of a comma cloud typically found with extratropical cyclones, while the subtropical cases show somewhat less organized precipitation structure and the maximum larger composite rain rates are greater than the midlatitude composite. In both cases the maximum precipitation is northeast of the center of the cross section.

Differences in the vertical structure between subtropical and midlatitudes ARs are also revealed by this analysis. The upper-level (ULJ) and low-level jets (LLJ) are both stronger in the midlatitude ARs, with the ULJ and LLJ averaging just over 50 and 25 m s^{-1} in the midlatitudes and 40 and 15 m s^{-1} in the subtropics.

Baroclinicity is evident in both sections (based on slope in the freezing level), but is greater in the midlatitudes. The atmosphere is generally cooler in the midlatitude cases, with the 0°C level averaging 3.3 and 1.8 km MSL on the south and north edges of the midlatitudes ARs, versus 4.2 and 3 km MSL for the subtropical ARs. Intriguingly, the AR core (as defined by either the largest IVT in the traces shown in the bottom panels, or by the largest low-level vapor transport in the cross sections in the top panels of Figs. 6, 8, and 10) is closer to the southern edge of the AR in the midlatitude cases than the subtropical ones, and the horizontal vapor transport in the AR core (as defined by the low-level vapor transport) is roughly 10% greater in the midlatitude cases. Both exhibit a slope poleward with height in terms of the location of maximum transport within the AR. Remarkably, the altitude beneath which 75% and 99%

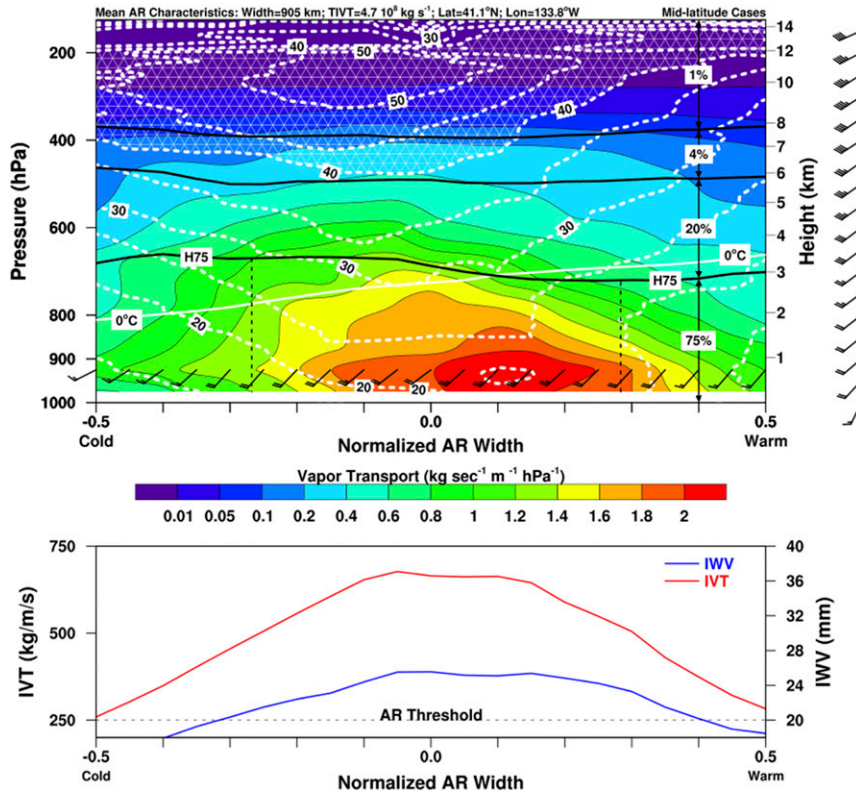


FIG. 10. As in Fig. 6, but for the 12 midlatitude cases.

of IVT occurs is nearly identical for the midlatitude and subtropical ARs.

d. Toward a scaling of AR water vapor transport

Given the vital role of ARs in both global water vapor transport and in creating extreme precipitation, there is potential value to both predictive and diagnostic studies in identifying, tracking, and communicating the relative magnitude of an AR event in terms of bulk water vapor transport. However, the units are rather hard to grasp without context. The development of a simple scale for AR strength can overcome this. This simple scale would be analogous to the existence of a “flood stage” for terrestrial streamflow and of the use of the “Sverdrup” for ocean current transport ($1 \text{ Sverdrup} = 10^6 \text{ m}^3 \text{ s}^{-1}$ of ocean current transport). The most analogous variable for ARs is TIVT, which ranges from 1.33 to $8.33 \times 10^8 \text{ kg s}^{-1}$ in the cases sampled here. Although this paper triples the number of such measurable cases available, it is clear that more extreme events exist but have not been observed. For convenience and simplicity, it could be useful to consider ranking ARs by their intensity in terms of multiples of 10^8 kg s^{-1} . Future work will identify the frequency of occurrence of AR intensities.

Experience suggests that maximum IVT (IVT_{MAX}) is another useful parameter that can help assess

the strength of an AR. Although it represents a single “point” in space and time, rather than a flux of an entire AR, the values are easily displayed on traditional weather maps. A comparison of IVT_{MAX}

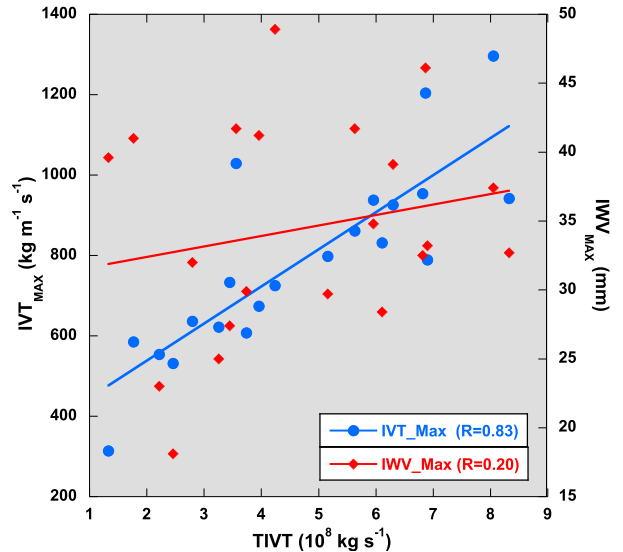


FIG. 11. Comparison of the IVT_{MAX} and IWV_{MAX} to the TIVT for each of the 21 cases listed in Table 1. The correlation between these values of IVT_{MAX} and TIVT is 0.83, and the correlation between IWV_{MAX} and TIVT is 0.20.

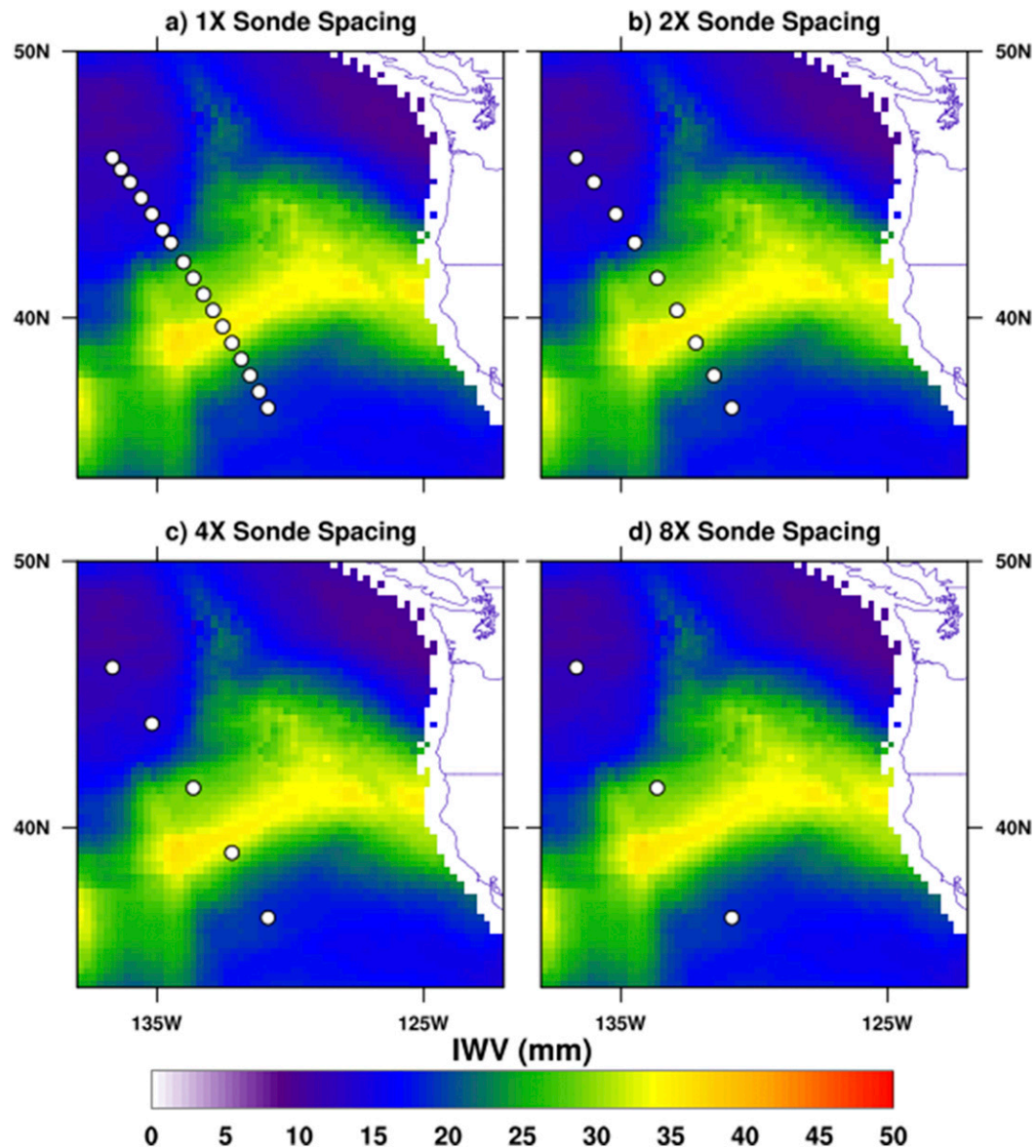


FIG. 12. Illustration showing how spacing between dropsondes was varied for resolution experiments using AR event 9 as an example. The white dots represent the locations of dropsondes. Shown are (a) the original spacing and spacing for the experiments with increased spacing of (b) 2 \times , (c) 4 \times , and (d) 8 \times . The background color fill shows IWV from SSM/I satellite measurements as described in Fig. 1.

with TIVT for the 21 cases shows an 83% correlation while maximum IWV (IWV_{MAX}) versus TIVT has a correlation of only 20% (Fig. 11). A comparison of IWV and IVT from all AR dropsondes (not shown) showed that increasing values of IVT are somewhat associated with increasing values of IWV; however, the correlation between the two parameters is relatively low at 0.53. Based on these results, the use of IWV as a proxy for IVT is not recommended.

e. Dropsonde horizontal resolution

The data from several well sampled cases are used to assess the sensitivity of AR transport (TIVT) to dropsonde horizontal spacing and vertical resolution. This sensitivity analysis is of practical importance for future field campaigns examining ARs because of the relatively high cost of the dropsondes.

In this sensitivity experiment, a series of sequential calculations of $TIVT_i$ ($i = 1 - N$) are made across

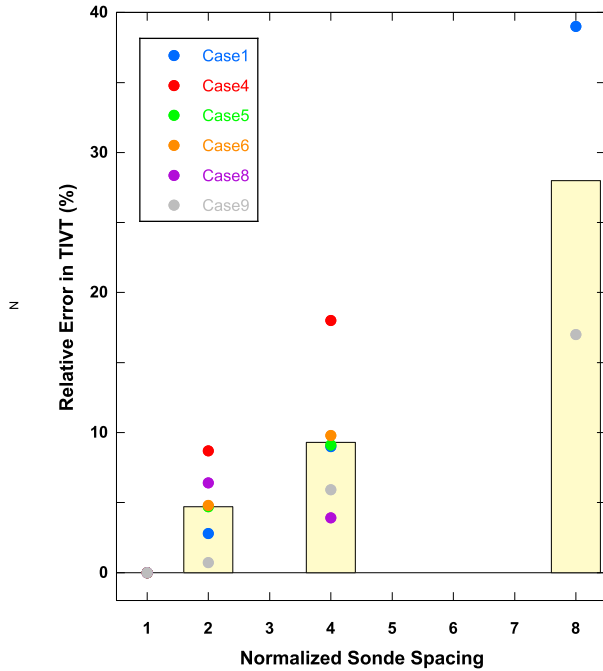


FIG. 13. Results from experiments examining the sensitivity of calculated TIVT to the spacing between dropsondes. The difference in TIVT between the control case (Δ TIVT) is shown as a function of the normalized dropsonde spacing (spacing relative to each respective control case; mean dropsonde spacing in these events varied from 63 to 95 km with a mean of 80 km). The circle markers show results from each individual case considered while the vertical bars show the mean across the cases.

an AR. The first calculation, $TIVT_1$, utilizes all available dropsondes and serves as the control. Subsequent calculations remove interior dropsondes so that the average distance between dropsondes doubles. Thus, the horizontal spacing would increase relative to the control case by a factor of 2 for $TIVT_2$, a factor of 4 for $TIVT_3$, a factor of 8 for $TIVT_4$, and so on (dropsondes on each end of the transect are the same throughout to ensure the width of the AR did not change).

For this experiment TIVT was calculated using the $IVT > 250 \text{ kg m}^{-1} \text{ s}^{-1}$ threshold. Only AR events 1, 4, 5, 6, 8, and 9 were used in this experiment because they had 1) a relatively uniform dropsonde spacing s across the AR ($\sigma_s / \langle s \rangle < 0.40$), where σ_s is the standard deviation of dropsonde spacing and 2) at least nine dropsondes across the AR allowing for an increased spacing of at least 4. The mean dropsonde spacing in each of these six AR events varied from 63 to 95 km with a mean of 80 km. Figure 12 shows how the sequential removal of specific dropsondes was performed to increase dropsonde spacing by a factor of 2, 4, and 8 using AR event 9 as an example.

When the spacing between dropsondes was doubled, the absolute difference in TIVT varied from 1% to 9% with a mean value of 5% (see Fig. 13). When the dropsonde spacing was increased by a factor of 4, the absolute TIVT difference from the control case ranged from 4% to 18%, although it should be noted that results from five of the cases varied from 4% to 10%, with a single case at 18%. The two experiments with enough dropsondes across the AR to allow an increase in spacing by a factor of 8 had a mean absolute difference of 28%.

A parallel experiment was carried using the 0.5° GFS analysis data described earlier. In this experiment, GFS analysis data were linearly interpolated to each dropsonde location, and then the procedure was carried out as before, that is, increasing the spacing between dropsonde sites by factors of 2, 4, and 8 and calculating the TIVT. Only three (events 6, 8, and 9) of the six cases were examined in this parallel experiment because of limited availability of 0.5° GFS analysis products.

The absolute differences in TIVT due to increasing spacing using the interpolated GFS analysis products was about one-third of the differences calculated when using the dropsonde values. The smaller differences are likely due to (at least in part) to 1) the interpolation of the GFS products to the dropsonde locations which would have a smoothing effect on horizontal variations and 2) numerical weather model products having (in general) smoother varying horizontal fields than the real atmosphere.

The results of this sensitivity experiment illustrate how the accuracy of the calculated TIVT across an AR degrades as the dropsonde resolution increases and may provide at least a first-order estimate for cost analyses during the planning of future research flights. Based on these results, it is recommended that future airborne AR experiments focused on TIVT normally use a dropsonde spacing of 100 km, which will not seriously degrade TIVT measurements and would on average still provide eight samples within AR conditions. Other AR science or objectives (e.g., numerical weather prediction and data assimilation) may require closer spacing.

f. Comparison to GFS analysis products

Dropsonde-derived values of IWV, IVT, and TIVT along transects from 14 AR cases were compared to values from GFS analysis products (0.5° grid) to provide an initial estimate on how well numerical models simulate these important quantities. Admittedly, the GFS model is just one of many numerical models, and the brief analysis provided here is simply a starting

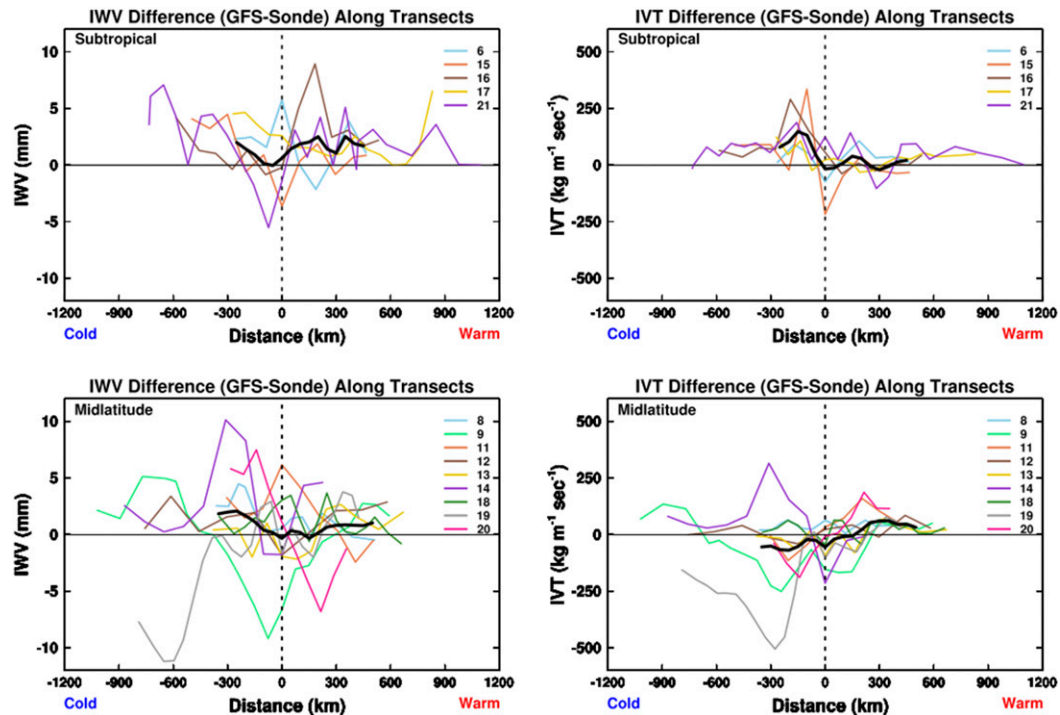


FIG. 14. Difference in (left) IWV and (right) IVT between dropsondes and GFS analysis products along 14 of the 21 AR transects. The thick black line in each panel represents the average over all transects. Transects are grouped by location: (top) subtropical and (bottom) midlatitude. The horizontal distance scale is referenced to the dropsonde location with the largest value of IWV or IVT in each transect. Transects are oriented with the cold end (generally toward the northwest) located on the left side of the plots.

point for a more comprehensive analysis involving multiple models.

Values of IWV and IVT were calculated using the GFS humidity and wind fields at each dropsonde location in the transects using linear interpolation and model analysis time closest to the time at midtransect.

Figure 14 shows the difference (GFS minus dropsondes) in IWV and IVT along 14 of the 21 AR transects shown in Table 1 (GFS products at 0.5° resolution were not available for cases 1–5, 7, and 10). In general, the GFS model overestimates both IWV and IVT in the subtropical cases and, to a lesser extent, in the midlatitude cases. There is a consistent trend for the GFS to overestimate IVT on the poleward side of subtropical ARs and on the southern side of midlatitude ARs.

Comparisons of TIVT calculated from the dropsondes and GFS model are found in Fig. 15. Values of TIVT calculated over the entire column (1000–300 hPa; Fig. 15a) show a relatively close correspondence between dropsondes and the GFS model, with the GFS model slightly overestimating TIVT (with the exception of a single outlier case), which is consistent with the results shown in Fig. 14.

Values of TIVT along each transect were calculated in 50-hPa layers to examine the vertical structure. The vertical profiles of this layer TIVT are shown in Fig. 15b, where the values are normalized by their respective TIVT calculated over entire atmospheric column. The difference between the layer TIVT vertical profiles shown in Fig. 15c indicate that the mean differences are up to about 2% of the total atmospheric column TIVT at any given height. However, there is a consistent trend for the GFS model to overestimate the TIVT contribution below about 925 hPa and above 550 hPa and to underestimate the TIVT contribution in between these pressure levels.

4. Discussion

Measurements from 21 AR events described above provide the best observations to date of the intensity, size, and structure of a relatively large number of ARs. This structure is summarized schematically in Fig. 16. Mean characteristics are shown based on using the IVT threshold of $250 \text{ kg m}^{-1} \text{ s}^{-1}$ to define the lateral boundary. The schematic highlights a type of

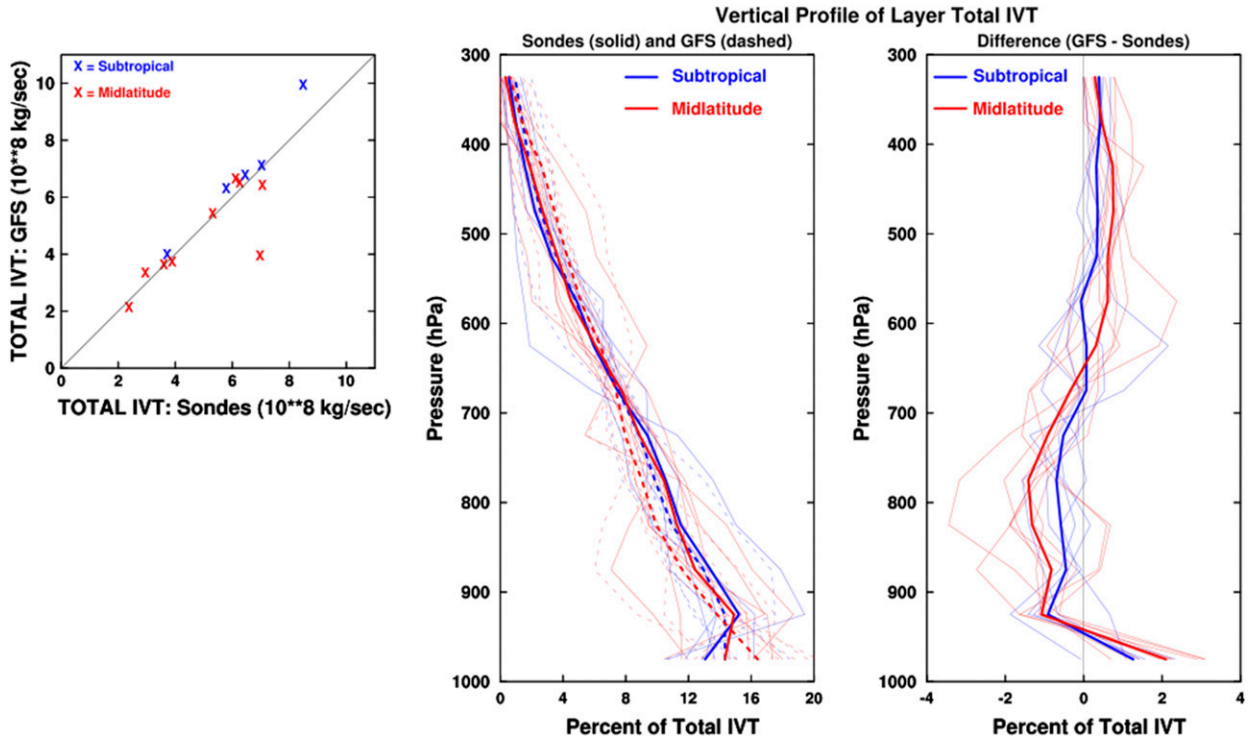


FIG. 15. Comparisons of TIVT across 14 AR transects from dropsondes and GFS analysis products. (left) Comparison between TIVT computed through the entire atmospheric column. (center) Comparison of vertical profile of TIVT calculated within 50-hPa layers from the dropsondes (solid lines) and GFS analysis (dashed lines). The results are normalized by the respective TIVT value calculated over the entire column. The thin lines represent individual subtropical (blue lines) and midlatitude (red lines) transects while the thick lines represent an average of all transects in each region. (right) The difference between dropsonde and GFS calculated values is shown, with thin lines denoting individual transects and thick lines representing the average of all transects in each region.

dipole structure in the vertical (Fig. 16b). The upper portion is the well-known upper-level jet, which is where the strongest winds are found, but where water vapor transport is minimal because of the extreme cold, and thus dryness of the air. The lower portion represents the atmospheric river, which carries the vast majority of the horizontal water vapor transport, even though the winds are not as strong as in the upper-level jet.

For each transect the total horizontal transport of water vapor within the domain of the AR was observed. It is analogous to a measurement of streamflow in a terrestrial river, which is measured in cubic meters per second. However, the flux in an AR is in the form of water vapor rather than liquid, the edges are less well defined, and TIVT is measured in kilograms per second. Another analogy is in terms of ocean currents and their transport of ocean water. Like ARs, they exist without solid lateral boundaries, and nonetheless measurements of their transport have been of great utility in ocean science.

Mean flow rate (i.e., TIVT) within the 21 observed ARs in Table 2 was about $4.7 \times 10^8 \text{ kg s}^{-1}$ with a maximum value of about $8.3 \times 10^8 \text{ kg s}^{-1}$. The width varied from 400 to 1400 km with a mean of 890 km (values based on IVT threshold). The average meridional water vapor flux in these 21 ARs was $3.1 \times 10^8 \text{ kg s}^{-1}$, or approximately 25% of the global average across 35°N as reported in Zhu and Newell (1998), thus suggesting that the mean of these 21 cases is representative of a global mean. The total instantaneous water vapor flux in an average AR is roughly equivalent to the flux of liquid water into the Gulf of Mexico from 27 Mississippi Rivers, or to the discharge of 2.6 Amazon Rivers (Kammerer 1990; see Table 3). For comparison, the total discharge of freshwater into the oceans is roughly $10^6 \text{ m}^3 \text{ s}^{-1}$ (Dai et al 2009; Seo et al 2012).

The results show that the relative importance of the wind field in producing an AR increases with latitude. At more subtropical latitudes, an AR may exist primarily because of very high concentrations of water

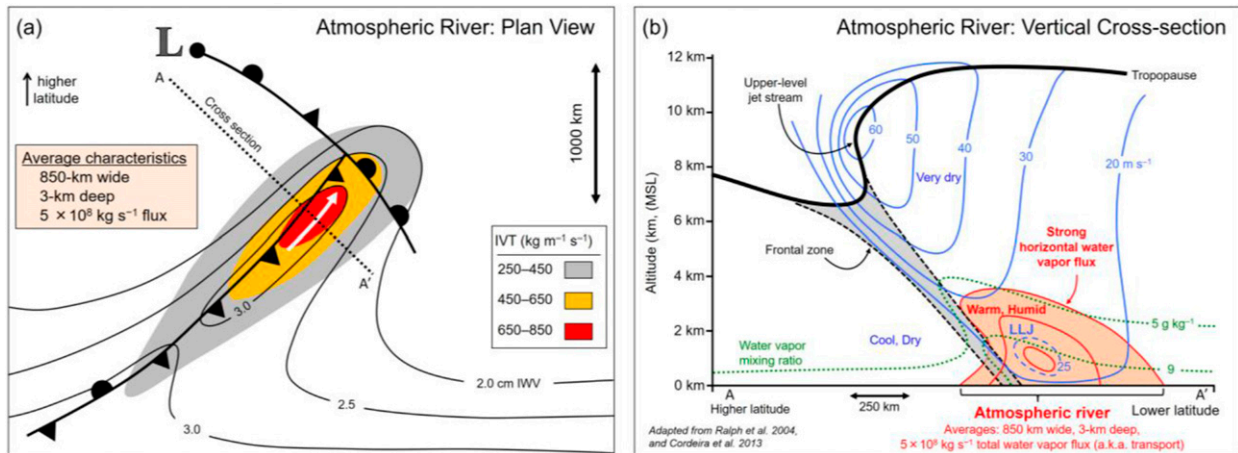


FIG. 16. Schematic summary of the structure and strength of an AR based on dropsonde measurements analyzed in this study, and on corresponding reanalyses that provide the plan-view context. (a) Plan view including parent low-pressure system and associated cold, warm, stationary, and warm-occluded surface fronts. IVT is shown by color fill (magnitude; $\text{kg m}^{-1} \text{s}^{-1}$) and direction in the core (white arrow). IWV (cm) is contoured. A representative length scale is shown. The position of the cross section shown in (b) is denoted by the dashed line A–A'. (b) Vertical cross-section perspective, including the core of the water vapor transport in the AR (orange contours and color fill) and the pre-cold-frontal LLJ, in the context of the jet-front system and tropopause. Water vapor mixing ratio (green dotted lines; g kg^{-1}) and cross-section-normal isotachs (blue contours; m s^{-1}) are shown. Magnitudes of variables represent an average midlatitude AR with lateral boundaries defined using the IVT threshold of $250 \text{ kg m}^{-1} \text{ s}^{-1}$. Depth corresponds to the altitude below which 75% of IVT occurs. Adapted primarily from Ralph et al. (2004) and Cordeira et al. (2013).

vapor, with relatively weak winds. As latitude increases toward the pole it becomes increasingly necessary to have both strong winds and adequate water vapor. In general, the AR width and TIVT are less dependent on latitude when IVT is used to define ARs than when IWV is used. Thus, IVT represents a more robust threshold across a wider range of conditions than does IWV.

The measurement of water transport rates in ocean currents has been routinely performed over many decades using vertical arrays of current meters. However, the more spatial and temporally transitory nature of ARs currently limits our observational methods over oceans to aircraft-deployed dropsondes, and over land to radiosondes and AR observatories (AROs; White et al. 2013). AROs include wind profiling radars and GPS-met IWV sensors that can monitor AR “bulk water vapor flux,” which is a proxy for IVT (Ralph et al. 2013). Seven AROs are now emplaced along the U.S. West Coast, and it is possible that more research aircraft missions will be conducted.

The emergence of the AR concept reflects an understanding that atmospheric horizontal water vapor transport in the midlatitudes and subtropics occurs almost entirely within relatively narrow “filaments.” There are typically 3–5 in existence in each hemisphere, each contributing roughly a quarter of the global water

vapor transport in the midlatitudes. Taken together, eight ARs globally transport an amount of water vapor equivalent to roughly 4 times the discharge of the world’s rivers.

It is envisioned that future work will use global reanalyses to evaluate the representativeness of the means derived from the airborne data presented here and will include quantitative evaluation of weather and climate reanalyses, forecasts, and climate projections through use of these unique observations. The increasing focus on the horizontal transport dimension of the atmospheric water vapor budget complements the

TABLE 3. Comparison of mean flow rates between the observed ARs in this study and major river systems. Mean river flow rates are from Wohl (2007), except for Mississippi River, which was taken from Kammerer (1990).

	Mean flow rate		Multiplier
	$10^9 \text{ m}^3 \text{ day}^{-1}$	$10^6 \text{ acre feet day}^{-1}$	
Average AR in this study	39.7	32.2	1 AR = X rivers
Largest AR in this study	71.7	58.2	
Amazon River	15.1	12.3	2.6
Congo River	3.6	2.9	11.0
Yangtze River	3.0	2.5	13.2
Mississippi River	1.5	1.2	27.4
Nile River	0.3	0.2	159

long-standing and extensive exploration of vertical water vapor fluxes from the Earth's surface and deep convection.

Acknowledgments. This research was supported by funding provided by Awards NA13OAR4830231 and NA13OAR4830271 from the National Oceanographic and Atmospheric Administration (NOAA). SSM/I data are produced by Remote Sensing Systems and data available at www.remss.com/missings/ssmi. GFS analysis products were downloaded from <http://emc.ncep.noaa.gov>. D.E.W.'s contribution to this study was carried out on behalf of the Jet Propulsion Laboratory, California Institute of Technology, under a contract with the National Aeronautics and Space Administration. The authors sincerely appreciate the input from three anonymous reviewers whose helpful suggestions and detailed comments greatly improved this manuscript.

REFERENCES

- Cordeira, J. M., F. M. Ralph, and B. J. Moore, 2013: The development and evolution of two atmospheric rivers in proximity to western North Pacific tropical cyclones in October 2010. *Mon. Wea. Rev.*, **141**, 4234–4255, doi:[10.1175/MWR-D-13-00019.1](https://doi.org/10.1175/MWR-D-13-00019.1).
- Dai, A., T. Qian, and K. E. Trenberth, 2009: Changes in continental freshwater discharge from 1948 to 2004. *J. Climate*, **22**, 2773–2792, doi:[10.1175/2008JCLI2592.1](https://doi.org/10.1175/2008JCLI2592.1).
- Demory, M.-E., P. L. Vidale, M. J. Roberts, P. Berrisford, J. Strachan, R. Schiemann, and M. S. Mizieliński, 2014: The role of horizontal resolution in simulating drivers of the global hydrological cycle. *Climate Dyn.*, **42**, 2201–2225, doi:[10.1007/s00382-013-1924-4](https://doi.org/10.1007/s00382-013-1924-4).
- Dettinger, M. D., 2013: Atmospheric rivers as drought busters on the U.S. West Coast. *J. Hydrometeorol.*, **14**, 1721–1732, doi:[10.1175/JHM-D-13-02.1](https://doi.org/10.1175/JHM-D-13-02.1).
- , F. M. Ralph, T. Das, P. J. Neiman, and D. Cayan, 2011: Atmospheric rivers, floods, and the water resources of California. *Water*, **3**, 445–478, doi:[10.3390/w3020445](https://doi.org/10.3390/w3020445).
- Environmental Modeling Center, 2003: The GFS atmospheric model. NCEP Office Note 442, 14 pp., <http://www.lib.ncep.noaa.gov/ncepooffice/notes/files/on442.pdf>.
- Guan, B., and D. E. Waliser, 2015: Detection of atmospheric rivers: Evaluation and application of an algorithm for global studies. *J. Geophys. Res. Atmos.*, **120**, 12 514–12 535, doi:[10.1002/2015JD024257](https://doi.org/10.1002/2015JD024257).
- , N. P. Molotch, D. E. Waliser, E. J. Fetzer, and P. J. Neiman, 2010: Extreme snowfall events linked to atmospheric rivers and surface air temperature via satellite measurements. *Geophys. Res. Lett.*, **37**, L20401, doi:[10.1029/2010GL044696](https://doi.org/10.1029/2010GL044696).
- , —, —, —, and —, 2013: The 2010/11 snow season in California's Sierra Nevada: Role of atmospheric rivers and modes of large-scale variability. *Water Resour. Res.*, **49**, 6731–6743, doi:[10.1002/wrcr.20537](https://doi.org/10.1002/wrcr.20537).
- Hughes, M., P. J. Neiman, E. Sukovich, and F. M. Ralph, 2012: Representation of the Sierra barrier jet in 11 years of a high-resolution dynamical reanalysis downscaling. *J. Geophys. Res.*, **117**, D18116, doi:[10.1029/2012JD017869](https://doi.org/10.1029/2012JD017869).
- Kammerer, J. C., 1990: Largest rivers in the United States. USGS Open-File Rep. 87–242, 2 pp., <http://pubs.usgs.gov/of/1987/ofr87-242/>.
- Kim, J., D. E. Waliser, P. J. Neiman, B. Guan, J.-M. Ryoo, and G. A. Wick, 2013: Effects of atmospheric river landfalls on the cold season precipitation in California. *Climate Dyn.*, **40**, 465–474, doi:[10.1007/s00382-012-1322-3](https://doi.org/10.1007/s00382-012-1322-3).
- Lavers, D. A., R. P. Allan, E. F. Wood, G. Villarini, D. J. Brayshaw, and A. J. Wade, 2011: Winter floods in Britain are connected to atmospheric rivers. *Geophys. Res. Lett.*, **38**, L23803, doi:[10.1029/2011GL049783](https://doi.org/10.1029/2011GL049783).
- , G. Villarini, R. P. Allan, E. F. Wood, and A. J. Wade, 2012: The detection of atmospheric rivers in atmospheric reanalyses and their links to British winter floods and the large-scale climatic circulation. *J. Geophys. Res.*, **117**, D20106, doi:[10.1029/2012JD018027](https://doi.org/10.1029/2012JD018027).
- Leung, L. R., and Y. Qian, 2009: Atmospheric rivers induced heavy precipitation and flooding in the western U.S. simulated by the WRF regional climate model. *Geophys. Res. Lett.*, **36**, L03820, doi:[10.1029/2008GL036445](https://doi.org/10.1029/2008GL036445).
- Mahoney, K., and Coauthors, 2016: Understanding the role of atmospheric rivers in heavy precipitation in the southeast United States. *Mon. Wea. Rev.*, **144**, 1617–1632, doi:[10.1175/MWR-D-15-0279.1](https://doi.org/10.1175/MWR-D-15-0279.1).
- Moore, B. J., P. J. Neiman, F. M. Ralph, and F. Barthold, 2012: Physical processes associated with heavy flooding rainfall in Nashville, Tennessee and vicinity during 1–2 May 2012: The role of an atmospheric river and mesoscale convective systems. *Mon. Wea. Rev.*, **140**, 358–378, doi:[10.1175/MWR-D-11-00126.1](https://doi.org/10.1175/MWR-D-11-00126.1).
- Neiman, P. J., F. M. Ralph, G. A. Wick, J. Lundquist, and M. D. Dettinger, 2008a: Meteorological characteristics and overland precipitation impacts of atmospheric rivers affecting the West Coast of North America based on eight years of SSM/I satellite observations. *J. Hydrometeorol.*, **9**, 22–47, doi:[10.1175/2007JHM855.1](https://doi.org/10.1175/2007JHM855.1).
- , —, —, Y.-H. Kuo, T.-K. Wee, Z. Ma, G. H. Taylor, and M. D. Dettinger, 2008b: Diagnosis of an intense atmospheric river impacting the Pacific Northwest: Storm summary and offshore vertical structure observed with COSMIC satellite retrievals. *Mon. Wea. Rev.*, **136**, 4398–4420, doi:[10.1175/2008MWR2550.1](https://doi.org/10.1175/2008MWR2550.1).
- , L. J. Schick, F. M. Ralph, M. Hughes, and G. A. Wick, 2011: Flooding in western Washington: The connection to atmospheric rivers. *J. Hydrometeorol.*, **12**, 1337–1358, doi:[10.1175/2011JHM1358.1](https://doi.org/10.1175/2011JHM1358.1).
- , G. A. Wick, B. J. Moore, F. M. Ralph, J. R. Spackman, and B. Ward, 2014: An airborne study of an atmospheric river over the subtropical Pacific during WISPAR: Dropsonde budget-box diagnostics and precipitation impacts in Hawaii. *Mon. Wea. Rev.*, **142**, 3199–3223, doi:[10.1175/MWR-D-13-00383.1](https://doi.org/10.1175/MWR-D-13-00383.1).
- Pierce, D. W., and Coauthors, 2013: The key role of heavy precipitation events in climate model disagreements of future annual precipitation changes in California. *J. Climate*, **26**, 5879–5896, doi:[10.1175/JCLI-D-12-00766.1](https://doi.org/10.1175/JCLI-D-12-00766.1).
- Ralph, F. M., P. J. Neiman, and G. A. Wick, 2004: Satellite and CALJET aircraft observations of atmospheric rivers over the eastern North Pacific Ocean during the El Niño winter of 1997/98. *Mon. Wea. Rev.*, **132**, 1721–1745, doi:[10.1175/1520-0493\(2004\)132<1721:SACAOO>2.0.CO;2](https://doi.org/10.1175/1520-0493(2004)132<1721:SACAOO>2.0.CO;2).
- , —, and R. Rotunno, 2005: Dropsonde observations in low-level jets over the northeastern Pacific Ocean from CALJET-1998 and PACJET-2001: Mean vertical-profile and

- atmospheric-river characteristics. *Mon. Wea. Rev.*, **133**, 889–910, doi:10.1175/MWR2896.1.
- , —, G. A. Wick, S. I. Gutman, M. D. Dettinger, D. R. Cayan, and A. B. White, 2006: Flooding on California's Russian River: Role of atmospheric rivers. *Geophys. Res. Lett.*, **33**, L13801, doi:10.1029/2006GL026689.
- , —, G. N. Kiladis, K. Weichman, and D. W. Reynolds, 2011: A multiscale observational case study of a Pacific atmospheric river exhibiting tropical–extratropical connections and a mesoscale frontal wave. *Mon. Wea. Rev.*, **139**, 1169–1189, doi:10.1175/2010MWR3596.1.
- , T. Coleman, P. J. Neiman, R. Zamora, and M. D. Dettinger, 2013: Observed impacts of duration and seasonality of atmospheric-river landfalls on soil moisture and runoff in coastal northern California. *J. Hydrometeorol.*, **14**, 443–459, doi:10.1175/JHM-D-12-076.1.
- , and Coauthors, 2016: CalWater field studies designed to quantify the roles of atmospheric rivers and aerosols in modulating U.S. West Coast precipitation in a changing climate. *Bull. Amer. Meteor. Soc.*, **97**, 1209–1228, doi:10.1175/BAMS-D-14-00043.1.
- Rutz, J. J., W. J. Steenburgh, and F. M. Ralph, 2014: Climatological characteristics of atmospheric rivers and their inland penetration over the Western United States. *Mon. Wea. Rev.*, **142**, 905–921, doi:10.1175/MWR-D-13-00168.1.
- Seo, K.-W., D. E. Waliser, B. Tian, B.-M. Kim, S.-C. Park, S. Cocke, B.-J. Sohn, and M. Ishii, 2012: Evidence of the recent decade change in global fresh water discharge and evapotranspiration revealed by reanalysis and satellite observations. *Asia-Pac. J. Atmos. Sci.*, **48**, 153–158, doi:10.1007/s13143-012-0015-5.
- Stohl, A., C. Forster, and H. Sodemann, 2008: Remote sources of water vapor forming precipitation on the Norwegian west coast at 60°N—A tale of hurricanes and an atmospheric river. *J. Geophys. Res.*, **113**, D05102, doi:10.1029/2007JD009006.
- Trenberth, K. E., J. T. Fasullo, and J. Mackaro, 2011: Atmospheric moisture transports from ocean to land and global energy flows in reanalyses. *J. Climate*, **24**, 4907–4924, doi:10.1175/2011JCLI4171.1.
- Viale, M., and M. N. Nunez, 2011: Climatology of winter orographic precipitation over the subtropical central Andes and associated synoptic and regional characteristics. *J. Hydrometeorol.*, **12**, 481–507, doi:10.1175/2010JHM1284.1.
- Waliser, D. W., and Coauthors, 2012: The “year” of tropical convection (May 2008 to April 2010): Climate variability and weather highlights. *Bull. Amer. Meteor. Soc.*, **93**, 1189–1218, doi:10.1175/2011BAMS3095.1.
- Wentz, F. J., K. A. Hilburn, and D. K. Smith, 2012: Remote Sensing Systems DMSP SSM/I Daily Environmental Suite on 0.25 deg grid, Version 7. Remote Sensing Systems, accessed 21 November 2016, www.remss.com/missions/ssmi.
- White, A. B., and Coauthors, 2013: A twenty-first-century California observing network for monitoring extreme weather events. *J. Atmos. Oceanic Technol.*, **30**, 1585–1603, doi:10.1175/JTECH-D-12-00217.1.
- Wick, G. A., P. J. Neiman, and F. M. Ralph, 2013: Description and validation of an automated objective technique for identification and characterization of the integrated water vapor signature of atmospheric rivers. *IEEE Trans. Geosci. Remote Sens.*, **51**, 2166–2176, doi:10.1109/TGRS.2012.2211024.
- Wohl, E. E., 2007: Hydrology and Discharge. *Large Rivers: Geomorphology and Management*, A. Gupta, Ed., John Wiley & Sons, 29–44, doi:10.1002/9780470723722.ch3.
- Zhu, Y., and R. E. Newell, 1998: A proposed algorithm for moisture fluxes from atmospheric rivers. *Mon. Wea. Rev.*, **126**, 725–735, doi:10.1175/1520-0493(1998)126<0725:APAFMF>2.0.CO;2.